Flame Acceleration and Transition to Detonation in an Array of Cylinders

Takanobu Ogawa[1*], Vadim N. Gamezo[2], Elaine S. Oran[2]

[1] Seikei University, 3-3-1 Kichijoji-Kitamachi, Musashino-shi, Tokyo 180-8633, Japan
[2] US Naval Research Laboratory, 4555 Overlook Ave., SW, Washington, DC 20375, USA

1 Introduction

The Deflagration-to-detonation transition (DDT) in reactive gases could occur in obstructed spaces. One configuration in which DDT might occur is a channel filled with obstacles. The prior studies [1,2] have shown that the geometry and layout of obstacles have significant effects on the flame acceleration and DDT in an obstructed channel. The flow over obstacles creates flow instabilities, which increase the flame surface area and the rate of energy release. The resulting thermal expansion accelerates the flow and the flame. Obstacles, however, also have an adverse effect on the flame acceleration, since the flow over an obstacle loses its momentum. In addition, obstacles reflect and diffract the shocks formed ahead of the flame, and thus they affect how and where detonation is ignited by the shocks.

We recently simulated DDT in an unconfined obstructed space, where a flame spreads cylindrically through a two-dimensional array of square obstacles [3,4]. In contrast to an obstructed channel, in which both obstacles and walls restrict the flow and wave propagation, the only restrictions in the unconfined array are created by obstacles. The result shows that the mechanism of flame acceleration and DDT is fundamentally the same as that in an obstructed channel, and there are also new phenomena that are not seen in a channel. For example, the flame speed is initially lower in some particular directions, and all DDT events occur in these directions. One explanation of this direction dependency is that the effects of obstacles are stronger in these directions than others.

To further study these phenomena, we have now simulated flame acceleration and DDT in an array of cylinders. In an array of square obstacles, the angle of attack, i.e., the angle between the flow and the edge of squares varies with the direction of flame propagation. Here, we use cylinders to exclude the effect of this varying angle of attack. For handling curvilinear geometry, we develop a solver based on an embedded boundary method.

2 Physical Model and Numerical Method

The governing equations are the two-dimensional, compressible, Navier-Stokes equations including convection, chemical reactions and energy release, molecular diffusion, thermal conduction, and viscosity. The equation of state is that of the ideal gas. The reaction model is based on one-step Arrhenius kinetics,

$$dY/dt = -\rho Y A_f \exp(-E_a/RT),$$

where Y is the mass fraction rate of the unburned material, A_f is the preexponential constant, and E_a is the activation energy. The thermal conductivity κ is approximated as $\kappa/C_p = \kappa_0 T^n$, where κ_0 and

Correspondence to: ogawa@st.seikei.ac.jp

$n = 0.7$ are model constants, and $C_p = \gamma R/W(\gamma - 1)$ is the specific heat. The Lewis number and the Prandtl number are assumed to be constant. The input parameters are calibrated to reproduce the laminar flame speed, the flame thickness, the detonation velocity, and the detonation cell size for the stoichiometric H_2-air mixture at 1 atm and 293 K [2].

This physical model is implemented on an adaptive Cartesian mesh using the Chombo library [5, 6], which provides data structures necessary for block-structured AMR. A multidimensional second-order Godunov method [7] is used for the inviscid terms, and the discretization of the diffusive terms is based on the central differencing. For curvilinear boundaries on a Cartesian mesh, Chombo uses an embedded boundary method, in which geometry is represented by volumes and apertures as shown in Fig. 1. The grey area in the figure represents a solid object and is excluded from the computation. At the embedded boundary segment, a stencil is extended normal to the boundary. The physical variables along the stencil are interpolated from the surrounding cells, and boundary values are calculated by using the stencil.

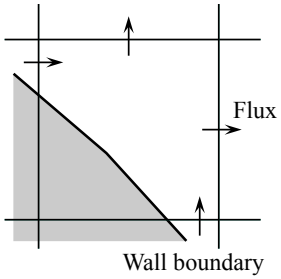

Figure 1: Embedded boundary method

3 Numerical Results

The computational configuration is shown in Fig. 2a. Cylinders 1 cm in diameter are evenly placed in a symmetric layout, and the distance between neighboring rows of the cylinders is 2 cm. A symmetry boundary condition is imposed at the left and the bottom boundaries of the computational region. The array is filled with a stoichiometric H_2-air mixture at 1 atm and 293 K, and the flow is initially at rest. We ignite the mixture by placing a small circular flame at the left-bottom corner of the computational domain. The finest mesh size is 1/128 cm, which corresponds to 4.5 computational cells within the laminar flame thickness.

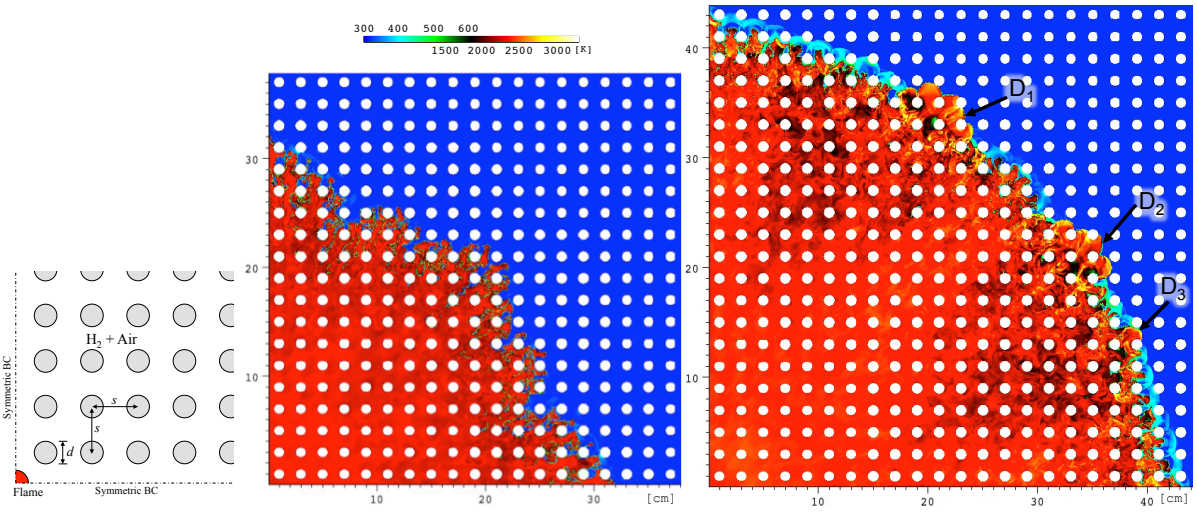

(a) (b) $t = 2.65$ ms (c) $t = 2.86$ ms

Figure 2: (a) The computational configuration of an array of cylinders. The diameter of a cylinder $d = 2$ cm, and the distance between the neighboring rows of cylinders $s = 2$ cm. (b) Temperature contours showing accelerating flame at 2.65 ms. (c) DDT events (denoted as D_i) at 2.86 ms.

The result of the computation is shown in Figs. 2b and 2c. After ignition, the flame propagates for some time in a laminar regime, and then it accelerates as its surface bends with the flow around the

cylinders. This contributes to an increase of the burning rate. The macroscopic shape of the expanding burned region does not become cylindrical but forms concave boundaries in some directions, as shown in Fig. 2b. This indicates that the flame speed is lower in these directions than others.

As the flow and flame accelerate, shocks are formed ahead of the flame. They are reflected by cylinders and propagate back to the flame, thus causing shock-flame interactions and further increasing the energy-release rate. This process strengthens the leading shocks. When they become strong enough, detonation is ignited behind the shocks reflected from cylinders in the unburned material near flame funnels. The simulation shows three independent DDT events within 90-degree sector, as shown in Fig. 2c. All the DDT events occurred in the directions where the concave boundaries of the burned region were formed (Fig. 2b).

Now, we study the dependency of flame speed on the direction of its propagation. In the cylindrically spreading flame shown in Fig. 2, the angle between the direction of flame propagation and the row of the array varies from one location to another, and flows in different directions interacts with each other. To see the effect of the angle, we consider the configuration shown in Fig. 3. An array of cylinders is rotated by an angle θ, and a planar flame propagates through the array. The rotation angle θ corresponds to the direction of flame propagation in the case of the cylindrically spreading flame.

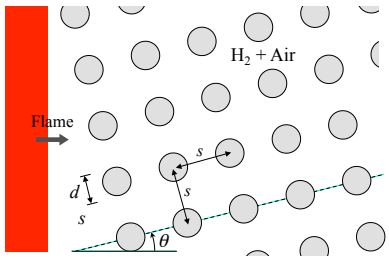

Figure 3: The configuration of a rotated array of cylinders. A planar flame is placed on the left.

Figure 4 shows the computational result of the early stage of flame propagation at 1.74 ms for the rotation angle $\theta = 0$, 14, and 45 degrees. The cylinder diameter $d = 1$ cm and the spacing between cylinders $s = 2$ cm are the same as those used in the computation shown in Fig. 2.

For $\theta = 0$ degrees, the flame propagates between the rows of cylinders without impinging on any cylinders, and thus the flame propagates faster than it would for other rotation angles. The flame is partially trapped by the wakes of cylinders, and the elongated flame surface also contributes to flame acceleration. On the other hand, for $\theta = 14$ and 45 degrees, the flame always impinges on cylinders, and the leading part of the flame is deformed by the flow around a cylinder. Impinging on cylinders causes significant momentum loss, and the resulting low flow speed delays the development of turbulence. Thus, the flame speed is lower in these more obstructed directions. For $\theta = 45$ degrees, long funnels of the unburned material are formed behind cylinders, and the resulting increase in the flame surface area is responsible for higher flame speed than that for $\theta = 14$

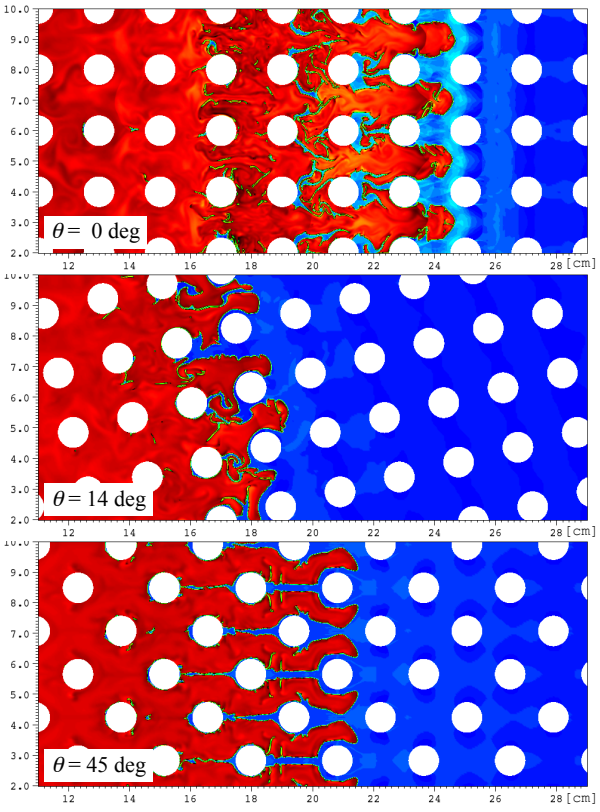

Figure 4: Accelerating flame in rotated arrays of cylinders. Temperature contours at 1.74 ms for angles of rotations $\theta = 0$, 14, and 45 degrees.

degrees. In the case of the cylindrically spreading flame, as shown in Fig. 2b, we observed the highest flame speed at $\theta = 0$ degrees and the concave boundaries of the burned material due to lower flame speed at $\theta = 14$ degrees. The momentum loss and the deformation of the flame surface vary with the angle, and this results in the different flame speed at different propagating angles in the early stage of flame propagation. As the flame propagates, however, shock-flame interactions become the dominant mechanism for flame wrinkling, and the flame can accelerate faster in more obstructed directions and this eventually leads to DDT in these directions.

Acknowledgments

This work was supported in part by a Grant-in-Aid from the Ministry of Education, Science and Culture of Japan (No. 21560188) and by the Naval Research Laboratory (NRL) through the Office of Naval Research. The computations were performed by using the RIKEN Integrated Cluster of Clusters (RICC) facility.

References

[1] A. Teodorczyk. Fast Deflagrations and Detonations in Obstacle-Filled Channels. *Biuletyn Instytutu Techniki Cieplnej Politechniki Warszawskiej*, 79:145–177, 1995.

[2] V.N. Gamezo, T. Ogawa, and E.S. Oran. Flame Acceleration and DDT in Channels with Obstacles: Effect of Obstacle Spacing. *Combustion and Flame*, 155:302–315, 2008.

[3] V.N. Gamezo, T. Ogawa, and E.S. Oran. Deflagration-to-Detonation Transition in Obstructed Spaces. In *22nd International Colloquium on the Dynamics of Explosions and Reactive Systems*, 2009.

[4] T. Ogawa, V.N. Gamezo, and E.S. Oran. Flame Acceleration and Transition to Detonation in an Array of Square Obstacles. In *Eighth International Symposium on Hazards, Prevention, and Mitigation of Industrial Explosions*, 2010.

[5] Chombo – Infrastructure for Adaptive Mesh Refinement. `https://seesar.lbl.gov/anag/chombo/`.

[6] P. Colella, D. T. Graves, T. J. Ligocki, D. F. Martin, D. Modiano, D. B. Serafini, and B. Van Straalen. Chombo Software Package for AMR Applications Design Document. `https://seesar.lbl.gov/anag/chombo/ChomboDesign-3.0.pdf`, 2009.

[7] P. Colella. Multidimensional upwind methods for hyperbolic conservation laws. *J. Comp. Phys.*, 87:171–200, 1990.